

# Phase Identification and Internal Stress Analysis of Steamside Oxides on Plant Exposed Superheater Tubes

**Pantleon, Karen; Montgomery, Melanie**

*Published in:*
Metallurgical and Materials Transactions A: Physical Metallurgy and Materials Science

*Link to article, DOI:*
10.1007/s11661-011-0874-x

*Publication date:*
2012

*Document Version*
Publisher's PDF, also known as Version of record

# Phase Identification and Internal Stress Analysis of Steamside Oxides on Plant Exposed Superheater Tubes

KAREN PANTLEON and MELANIE MONTGOMERY

During long-term, high-temperature exposure of superheater tubes in thermal power plants, various oxides are formed on the inner side (steamside) of the tubes, and oxide spallation is a serious problem for the power plant industry. Most often, oxidation in a steam atmosphere is investigated in laboratory experiments just mimicking the actual conditions in the power plant for simplified samples. On real plant-exposed superheater tubes, the steamside oxides are solely investigated microscopically. The feasibility of X-ray diffraction for the characterization of steamside oxidation on real plant-exposed superheater tubes was proven in the current work; the challenges for depth-resolved phase analysis and phase-specific residual stress analysis at the inner side of the tubes with concave surface curvature are discussed. Essential differences between the steamside oxides formed on two different steels typically applied for superheaters, ferritic-martensitic X20CrMoV12-1 and lean austenitic stainless steel TP347H, respectively, are revealed by X-ray diffraction.

DOI: 10.1007/s11661-011-0874-x


## I. INTRODUCTION

THE long-term service of superheater tubes in thermal power plants results in high-temperature fireside corrosion of the outer surface and steamside oxidation of the inner surface of the tubes. Often, steamside oxides consist of both oxide layers formed by outward growth on top of the original steel surface (outer oxide) and an oxidation zone beneath the steel surface (inner oxide zone). Understanding the mechanisms of oxide formation and scale growth in steam atmospheres at high temperatures and high internal pressures is of both academic and economic interest. A serious concern of the power plant industry is spallation of the steamside oxide scale[1–3] because it can provoke unforeseeable shutdowns and decrease the lifetime of components in the plants. Oxide flakes originating from the spallation of steamside oxides result in blockage of loops, which can cause insufficient steam flow and, finally, failure by overheating of the tubes. Furthermore, exfoliated oxide flakes get carried away with the steam and can cause erosion of downstream components like turbine blades. To monitor the formation of steamside oxides in power plants, parts of the superheater tubes are replaced during regular inspections, and the morphology of the oxide scale on these service-exposed tubes is investigated. To this end, almost exclusively light and electron microscopy studies supplemented by local analysis of the chemical composition are usually carried out on the plant exposed components. Such microscopy-based investigations reveal important information on the thickness of the oxide scale, on the distribution of (multi)layers or localized precipitations, and on the microstructure of the steel beneath the oxide scale.[4–6] However, a conclusive interpretation of the microscopic observations including thorough identification of various phases based on contrast or morphological differences in micrographs either requires long-standing experience or additional information from well-defined laboratory experiments. Systematic laboratory studies on the effect of different steam conditions (*e.g.,* temperature and heat flux) on the formation of oxide phases and the kinetics of scale growth contributed considerably to understanding steamside oxidation during the past decades,[7] in particular because dedicated characterization tools (like X-ray diffraction [XRD]) supplementing microscopic investigations can often be applied straightforwardly on the simple geometries of laboratory samples such as metallic coupons, whereas this is less feasible on the real exposed components. Conclusions, however, solely based on laboratory studies are questionable[8,9] and the difficulty of mimicking real service conditions in the laboratory becomes particularly obvious in the present case of high temperature exposure in the power plant. The following uncertainties and limitations for the comparability of laboratory and plant exposure are relevant for the problem of oxide spallation after high-temperature corrosion.

### A. *Exposure Conditions*

The actual temperature, which the superheaters experience in the plant during service, is usually unknown. It can be considerably different at various positions on the tube in longitudinal and circumferential direction, and it

KAREN PANTLEON, Associate Professor, is with the Department of Mechanical Engineering, Technical University of Denmark, Kemitorvet, Building 204, DK-2800 Kgs. Lyngby, Denmark. Contact e-mail: kapa@mek.dtu.dk MELANIE MONTGOMERY, Senior Scientist, is with the Department of Mechanical Engineering, Technical University of Denmark, and is also with Vattenfall A/S, Thermal Engineering Denmark, Stoeberigade 14, 2450 Copenhagen, Denmark.
Manuscript submitted June 21, 2011.
Article published online September 10, 2011

may increase gradually over several years as a consequence of oxide scale thickening.[10,11] Often, the steel temperature during service exposure is estimated only afterward based on the measured thickness of grown oxide scales, but apart from the uncertain assumptions on the kinetics of scale formation, this cannot account for already occurred spallation. Calculations of the temperature at the steel surface based on measurements of the steam temperature at the inlet and outlet of the loops are also difficult because additional information on the pressure, heat flux, and flow rate of the steam, as well as the influence of already formed oxide phases, needs to be considered[11,12]; the corresponding phases, however, are often unknown. Enormous temperature gradients were calculated for plant exposed tubes[1,13] as a consequence of huge temperature differences between the combustion gas and the steam.

In many cases, spallation is observed only after long-term exposure over several years (several thousand hours of operation[14]), which is not feasible for exposure experiments in the laboratory. Extrapolation toward industrial long-term exposure may fail because the oxidation mechanism and, hence, the kinetics of scale growth, can change with time.[15]

Most oxide scale failure occurs as a consequence of temperature changes because of regular or unexpected shutdowns during the lifetime of superheaters, which is a key factor for the evolution of stresses in the oxide scale. In addition to temperature variations, boiler shutdowns also cause changes in steam pressure in the superheater tubes.[12] Although thermal cycling and pressure fluctuations, in principle, can be considered also in laboratory experiments, the real exposure conditions can hardly be mimicked.

### B. *Sample Conditions*

For the plant exposed tubes, steamside oxidation on the inner side of the tubes, *i.e.,* the concave surface, is of interest. Most laboratory studies, however, fully neglect the influence of the surface curvature by using flat metal sheets in laboratory furnace experiments (sample curvature is often only considered in a theoretical manner). The sample geometry, however, considerably influences the formation and, consequently, the magnitude and sign of growth stresses and thermal stresses in the oxide scale.[1,12,13,16–18] As a consequence of its effect on stress formation, the surface curvature of the sample also affects the kinetics and the morphology of the growing oxide.[19–21]

In addition to the different stress states in planar *vs* nonplanar samples, the surface topography and the microstructure of laboratory samples is usually different from real superheater tubes. The flat laboratory samples may be deformed by machining (grinding and/or polishing), and the resulting lattice defects enhance diffusion in the surface near region strongly. As a result, the formation of protective oxide phases (like $Cr_2O_3$) is considerably favored for the mechanically prepared laboratory samples compared with real superheater tubes and, consequently, the resistance of laboratory samples to high-temperature oxidation is often much better compared with real service exposure. Furthermore, for laboratory samples, often the chemical composition is simplified also, and pure iron or model alloys with selected alloying elements of well-defined concentrations are used for many laboratory experiments.

The current study reports on steamside oxidation on real service exposed superheater tubes. Oxide scale formation on the steamside of superheater tubes is investigated by means of X-ray diffraction, and the differences with respect to phase composition and phase-dependent residual stresses are discussed for two typical boiler steels.

## II. EXPERIMENTAL

### A. *Plant-Exposed Superheater Tubes*

Superheater tubes exposed in Danish thermal power plants were investigated in the current work. They were replaced during regular service inspection after long-term exposure before failure had occurred. The tubes represent two typical types of superheaters, a ferritic-martensitic steel X20CrMoV12-1 and a lean austenitic stainless steel TP347H (Table I). The steel TP347H was available in two different grades, a fine-grained version (ASTM number 8, *i.e.,* grain size of approximately 25 $\mu$m) and a coarse-grained version (ASTM number 5-6 corresponds to 50 to 75-$\mu$m large grains). Table II summarizes the exposure conditions and dimensions of the plant-exposed superheater tubes.

For experimental characterization of the steamside oxides, ring samples were cut from the long superheater tubes received from the power plants.

### B. *X-Ray Diffraction*

XRD analysis was performed applying a diffractometer D8 Discover (Bruker AXS, Karlsruhe, Germany). An Eulerian cradle enabled sample rotations by the azimuth angle $\varphi$ and sample tilts by the pole angle $\psi$. Grazing incidence geometry applying a thin film attachment allowed measurements with limited penetration

**Table I. Chemical Composition of Plant Exposed Superheater Tubes**

| | Main Alloying Elements (wt pct) | | | | | | | |
|---|---|---|---|---|---|---|---|---|
| | C | Cr | Ni | Mn | Mo | V | Nb | Si |
| X20CrMoV12-1 | 0.17–0.23 | 10.0–12.5 | 0.3–0.8 | <1.0 | 0.8–1.2 | 0.25–0.35 | — | <0.5 |
| TP347H | 0.04–0.10 | 17.0–20.0 | 9.0–13.0 | <2.0 | — | — | 0.80–1.0 | <1.0 |

Table II. Geometry (Inner Diameter, $d_{inner}$, and Wall Thickness, $D_{wall}$) and Exposure Conditions (Steam Temperature $T_{steam}$, Exposure Time $T$, Number of Shutdowns $N$ Per Year) for the Service-Exposed Superheater Tubes

| | Geometry | | Exposure | | | | |
|---|---|---|---|---|---|---|---|
| Steel and Sample Name | $d_{inner}$ (mm) | $D_{wall}$ (mm) | $t$ (h) | $T_{steam}$ (K) | $p_{steam}$ (bar) | $N$ | Comments |
| X20CrMoV12-1 | | | | | | | |
| X20-1 | 18.2 | 6.7 | 31000 | 833 | 255 | 5–15 turbine starts | |
| X20-2 | 18.8 | 7.6 | 16000 | 833 | 255 | 5–15 turbine starts | |
| TP347H | | | | | | | |
| fine-grained: TP-FG | 21.7 | 7.8 | 30000 | 843 | 250 | 1 boiler start | |
| coarse-grained: TP-CG-1 | 21.7 | 5.9 | 5000 | 857 | 91 | 200 boiler starts | no heat flux |
| coarse-grained: TP-CG-2 | 21.7 | 4.6 | 5000 | 869 | 91 | 200 boiler starts | |

Table III. Penetration Depth of the X-Ray Beam as a Function of the Wavelengths (Cr-Kα and Co-Kα) and the Diffraction Geometry (BB – Conventional Bragg-Brentano-Diffraction, GI – Grazing Incidence Diffraction with Incidence angles γ). Values Represent Averages for the Oxides Hematite and Magnetite Assuming Similar Absorption of X-rays by Both Phases

| | Cr-Kα (36 ≤ deg 2Θ ≤ 160) | Co-Kα (20 ≤ deg 2Θ ≤ 120) |
|---|---|---|
| BB | 3.2 … 10.3 μm | 3.6 … 18.1 μm |
| GI | | |
| γ 5 deg | 1.6 μm | 2.7 … 3.3 μm |
| 10 deg | 2.6 μm | 3.6 … 6.1 μm |
| 15 deg | 3.1 … 3.7 μm | 2.7 … 8.5 μm |
| 20 deg | 3.2 … 4.7 μm | 10.6 μm (120 deg 2Θ) |

*GI*, grazing incidence diffraction with incidence angles γ.

depths of the X-ray beam and, furthermore, the advantage of constant penetration depth over the whole range of measured diffraction angles. Systematic combinations of the diffraction technique (conventional *vs* grazing incidence applying different incidence angles) with different applied wavelengths (Cr-Kα and Co-Kα) of the X-rays allowed variations of the X-ray information depths as shown in Table III. As the thickness of the oxide scales (which, for the present samples, is up to 250 μm) exceeded the maximum X-ray information depth, the nondestructive measurements were combined with stepwise removal of the surface. A suitable method for removing the oxide scale on the concave surfaces of the samples for depth-resolved diffraction analysis has to meet the following demands: (1) During each removal step, a few tenths of micrometers should be removed homogeneously in depth; (2) surface roughness should be minimal, in particular, for grazing incidence XRD; (3) the removed materials should be applicable as reference material for correcting measurements on the real samples and possible alignment errors. Various removal techniques were tested. By chemical removal and applying $HNO_3$, only a selective attack of the sample was observed, and consequently, inhomogeneous layer thicknesses were removed in each step. Furthermore, by chemical dissolution, the removed material was lost in the liquid reagent and could not be used for XRD analysis. The usefulness of mechanical grinding was found to depend strongly on the grit size of the grinding paper: The best results were obtained with fine paper of grit 4000, whereas for larger grit sizes, increased amounts of SiC particles originating from the grinding paper were mixed with the removed oxide particles and considerably hindered XRD phase analysis on the powders. In particular during the first removal steps, the outer—surface near—oxide layers on the steamside of the tubes were highly susceptible to spallation and allowed straightforward layer-wise removal with well-defined homogeneous thicknesses. The mechanically removed thicknesses were calculated from the corresponding weight differences of the samples assuming precise knowledge of the sample area and uniform removal along that area.

The concave surface of the tubes, *i.e.,* the steamsides, were subjected to phase analysis and lattice strain measurements. To access the concave surfaces (the inner side of the tubes) by XRD, ring samples were cut from the tubes (see also the next section).

For a phase analysis, the ring samples were cut into segments, which improved the accessibility of the concave surface during the measurement considerably; however, cutting of the segments affected the state of internal stresses drastically, which, however, did not hinder phase identification. A phase analysis was performed first on the original surface and successively on the surfaces after each removal step applying both conventional Θ-2Θ measurements and grazing incidence measurements with various incidence angles of the X-ray beam. Because the thickness of removed layers was always larger than the X-ray penetration depth, an absorption correction of the measured intensities was not applied, and measurements after each removal step are assigned to the corresponding penetration depth. The removed material obtained after each removal step was used in form of powders for measurements of the stress-free reference state.

Stress analysis on the concave surfaces on the inner side of the ring samples is tricky. Cutting a ring from a tube has to meet two demands: On the one hand, the width of the ring sample should be as large as possible to minimize the effect of cutting; on the other hand, the ring should be as thin as possible, to avoid shading effects of the X-ray beam on its way to the inner surface of the ring, which is a problem in particular for high-diffraction angles as required for accurate stress measurements. A compromise between the two contradicting demands was applied, and the resulting widths of the rings amounted to approximately 10 mm. Shading effects according to the ring shape of the sample restricted the possible sample rotation around its surface normal by the azimuth angle $\varphi$ and the sample tilt by the pole angle $\psi$ being the angle between the normal of the sample and the lattice plane normal. Hence, complete XRD stress determination (tensor analysis) is not possible for measurements at the inner side of the rings. XRD stress analysis is based on the experimental determination of lattice strain $\varepsilon_{hkl}^{\phi,\psi}$ by recording the angular shift of a given reflection as a function of specimen tilt $\psi$ and rotation $\varphi$ and the measured lattice strain is related to the biaxial stress state consisting of $\sigma_1$ and $\sigma_2$ according to[22]

$$\varepsilon_{hkl}^{\phi,\psi} = s_1(\sigma_1 + \sigma_2) + \frac{1}{2}s_2\left(\sigma_1 \cos^2\phi \sin^2\psi + \sigma_2 \sin^2\phi \sin^2\psi\right) \quad [1]$$

The stress $\sigma_1$ represents the circumferential stress, which was obtained from measurements at $\varphi = 0$ deg with $0 \le \psi \le 45$ deg. Because of the ring shape of the samples and the need to measure on its concave (inner) side, the measurements at $\varphi = 90$ deg required tilting the sample by at least 25 deg to avoid shading; thus, the stress $\sigma_2$ was obtained at $\varphi = 90$ deg with $25 \le \psi \le 55$ deg. For stress calculation of the $\sigma_2$ components, additionally, the $\psi = 0$ data measured at $\varphi = 0$ deg were included because the values in the untilted sample state must be independent of the sample rotation. The stress $\sigma_2$ corresponds to the stress component in the longitudinal direction of the ring, but because the ring was cut from the tube, it does not represent the longitudinal stress of the entire tube. Although a radial stress component $\sigma_3$ can be expected for the current samples because of their surface curvature,[23] its maximum value lies at the interface between the outer oxide and the steel and is not accessible from the XRD measurements because of the rather low penetration depths of the X-rays. Also, because of stress relaxation at the surface, the radial stress component can be neglected here. Furthermore, Eq. [1] assumes the absence of shear stresses, which is a reasonable assumption for the current ring shape of the samples.

The X-ray elastic constants (XECs) $s_1$ and $\frac{1}{2}s_2$ were calculated for the magnetite phase according to the Hill-model applying the single elastic constants of the (731) lattice planes of magnetite[24] $s_1^{731} = -1.15\ 10^{-6}$ MPa$^{-1}$ and $\frac{1}{2}s_2^{731} = 5.33\ 10^{-6}$ MPa$^{-1}$. In the absence of available data for the hematite phase, macroscopic elastic constants[23] were used for calculating the XEC values of hematite: $s_1 = -0.90\ 10^{-6}$ MPa$^{-1}$ and $\frac{1}{2}s_2 = 5.66\ 10^{-6}$ MPa$^{-1}$.

A special sample holder was manufactured for the precise mounting of the ring samples within the diffractometer. Phase-specific stresses were determined: For hematite, measurements corresponding to the 226 reflection were performed, and for magnetite, the 731 reflection was measured. Both diffraction line profiles were recorded simultaneously from one and the same measurement covering both diffraction angles (H-226: 108.33 deg 2Θ, M-731:109.81 deg 2Θ). The measured diffraction line profiles were evaluated by pseudoVoigt fitting.

## III. RESULTS AND DISCUSSION

### A. *Phase Formation on the Steamside of Superheater Tubes*

X-ray diffractograms measured on the concave (steamside) surfaces of both the ferritic-martensitic X20CrMoV12-1 and the austenitic TP347H superheater tubes are shown in Figure 1. Apparently, the Bragg angles of measured line profiles correspond well with the theoretical values expected for the iron oxides $Fe_2O_3$ (hematite) and $Fe_3O_4$ (magnetite); see Figure 1. However, a detailed evaluation of the line profiles and measurements after successive film removal reveals considerable differences between the two types of steels, as discussed in the next section.

#### 1. *Ferritic-martensitic superheater tubes*

For the two different X20CrMoV12-1 superheater tubes in this study, an XRD phase analysis revealed

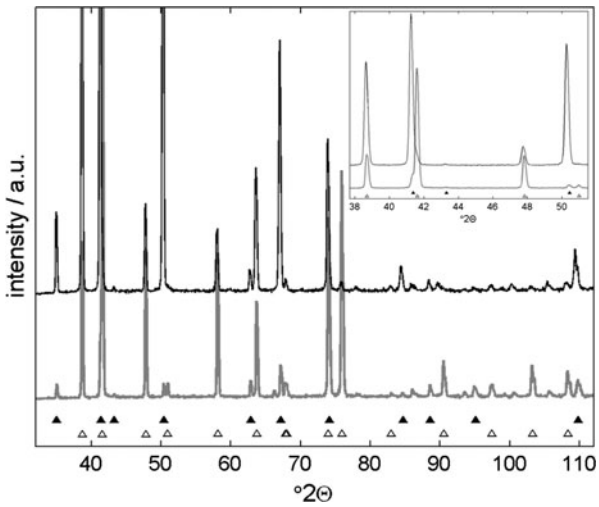


Fig. 1—X-ray diffractograms measured on the concave surface (steamside) of plant exposed superheater tubes: samples X20-1 (gray) and TP-CG-1(black); magnification of a selected range of diffraction angles is shown in the upper right corner. The theoretical positions of Bragg angles corresponding to hematite (open triangles) and magnetite (closed triangles) are marked (JCPDS card numbers: 86-0550 and 82-1533, respectively); all additional peaks of low intensity also belong to these phases, but for the sake of clarity, they are not marked by symbols.

similar results, and measurements at various locations on the ring samples indicated the presence of the same phases in all cases; only slight thickness variations were observed for the various phases as indicated by changes of the diffraction intensities of the various peaks. A depth-dependent phase analysis on the concave side of the X20CrMoV12-1 sample (for the sake of clarity, Figure 2 shows only a selected range of measured diffraction angles) revealed that the steamside oxide on the superheater tube consists of hematite only in the near surface region.

Already after the second removal the intensities measured for hematite reflections decrease drastically and at about 41 $\mu$m beneath the surface, only weak intensities indicating a lower fraction of hematite were measured. At greater depths, where hematite was absent, only diffraction lines apparently corresponding to magnetite were detected. A detailed evaluation of individual peaks, however, revealed considerable changes with depth. In contrast to the fully symmetrical line profiles measured on the surface and after the first removal step, asymmetric peaks were recorded after subsequent removal (Figure 3 shows an example). In general, asymmetric peaks can originate from differences in the chemical composition and/or stress gradients perpendicular to the surface. Two observations seem to be important for understanding the line profile asymmetry of the current sample. At exactly the depth where asymmetric broadening of line profiles was measured for the first time (after the third removal step, 104 $\mu$m), different characteristics of the oxide layer during removal were observed. Whereas removed powder, directly underneath the hematite layer, appeared black and initially was easy to remove (indicating weak adherence to the surface), it was more difficult to continue oxide removal, and a greasy black powder was obtained. A chemical element analysis applying energy dispersive spectroscopy (EDS) on the surface in the scanning electron microscope after that removal revealed approximately 6 wt pct chromium on the greasy surface, whereas chromium was absent on the overlying surfaces with loosely adherent oxide. The magnetite phase can contain chromium in solid solution, resulting in the spinel $(Fe,Cr)_3O_4$ as a compact layer with improved adhesion.[25] The lattice parameter of the chromium-containing spinel does not obey Vegard's law, but it shows a sigmoid dependence on composition[26–28] with increased lattice parameters in the range of 6 to 9 wt pct chromium and, hence, correspondingly decreased Bragg angles compared with pure magnetite. Alternatively, solid solution of manganese in the spinel also would shift reflections toward lower diffraction angles,[27] but only a slight increase of the manganese concentration at the interface between the outer and the inner oxide was measured by EDS. The asymmetric diffraction line profiles were evaluated based on the assumption that each profile measured as a function of depth reflects two different face-centered cubic phases (indeed, two distinct peaks were visible in each profile), and the evolution of the lattice parameters was estimated for both phases from their corresponding Bragg angles. The results indicate that the outer oxide layer contains pure magnetite, whereas the inner layer beneath the original surface of X20CrMoV12-1 consists of a mixture of magnetite and solid solutions with gradually increasing lattice parameters (Figure 4). Although the current assumption of two individual phases and corresponding overlap of the line profiles is not fully correct, because in the presence of chemical gradients each diffraction line profile reflects many

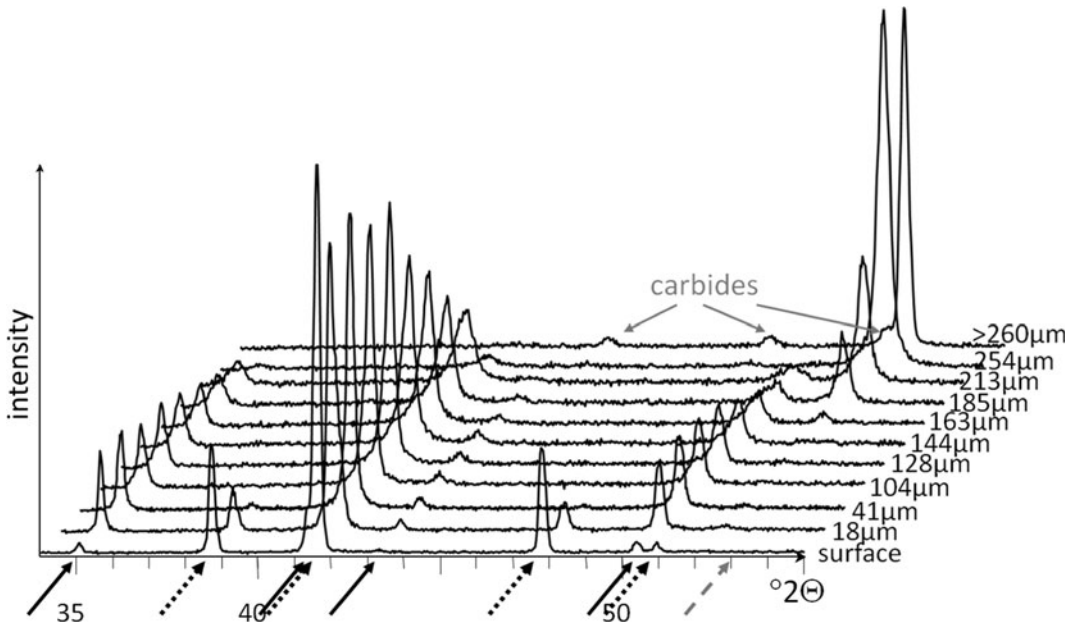


Fig. 2—X-ray diffractograms measured on the concave surface (steamside) after successive oxide removal for the X20CrMoV12-1 superheater tube (sample X20-1). The phases of hematite (dotted arrow), magnetite (black arrow), and $\alpha$-iron (gray dashed arrow) are marked, and the distances from the original surface corresponding to the various removal steps are indicated.

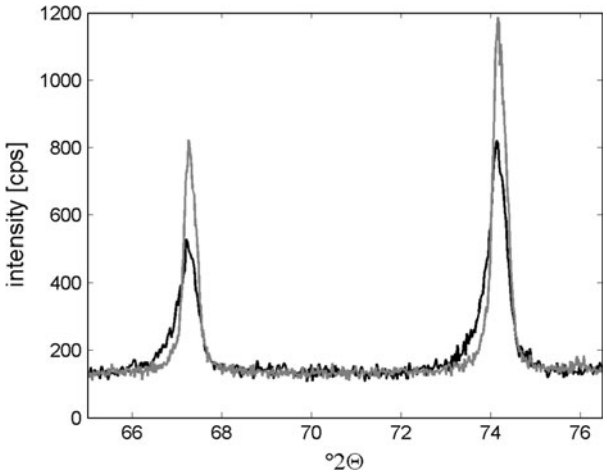


Fig. 3—Example of line profiles measured after the second (41 $\mu$m, gray) and the fifth (144 $\mu$m, black) removal of the steamside oxide on X20CrMoV12-1. The intensity maxima correspond to the magnetite phase.

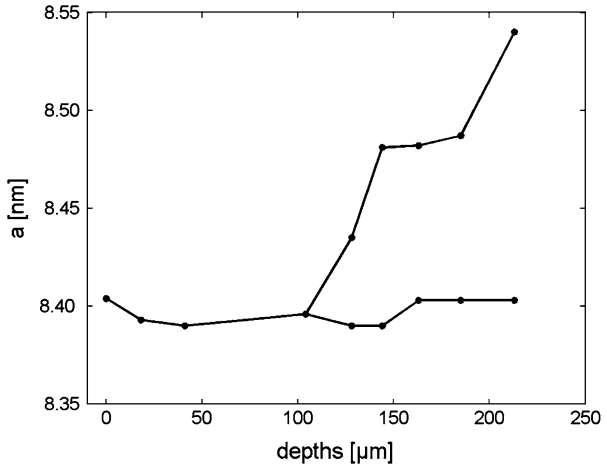


Fig. 4—Depth dependence of the lattice parameters calculated from measurements after stepwise removal of the steamside oxide scale on X20CrMoV12-1. The occurrence of two distinct lattice parameters indicates the simultaneous presence of two spinel phases.

layers of isostructural oxides with slightly different chemical composition in each layer, which, however, cannot be resolved by XRD, the obtained lattice parameters agree well with the expected values for chromium and manganese-containing spinel.[27] The coexistence of both the pure magnetite and the spinel with a solid solution of steel-alloying elements (Figure 4) suggests that the solid-solution spinel represents local regions in a magnetite matrix beneath the original steel surface, which agrees with microscopic observations.[15,29] With subsequent film removal, diffraction lines corresponding to oxide phases become weaker, and simultaneously, an increasing intensity originating from the $\alpha$-iron phase of X20CrMoV12-1 was measured. At approximately a 260-$\mu$m distance from the surface, additionally, $Cr_{23}C_6$ carbides were detected (Figure 5). Although carbides of the $M_{23}C_6$ type are typical for the steel X20CrMoV12-1 and they should be present

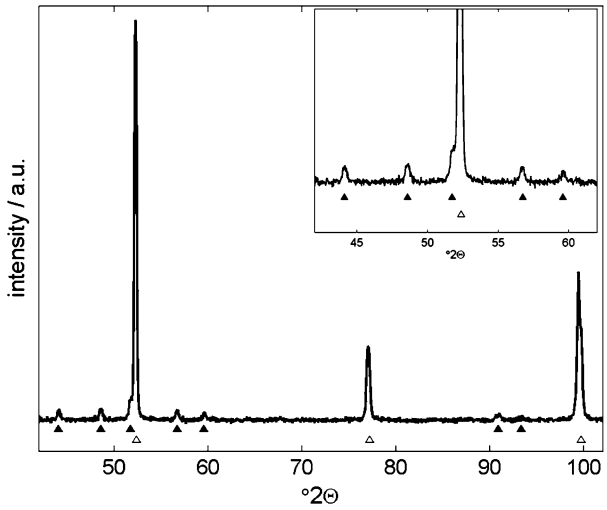


Fig. 5—X-ray diffractogram measured on the concave (steamside) surface of X20CrMoV12-1 after removal of approximately 260 $\mu$m from the original surface; the magnification of a selected range is shown in the upper right corner. The theoretical positions of Bragg angles corresponding to $Cr_{23}C_6$ carbides (closed triangles) and $\alpha$-iron (open triangles) are marked.

throughout the whole sample, they were detected neither in the oxide scale nor in the bulk away from the oxidized surfaces of the current samples. It has been shown previously that coarsening of the carbides occurs during long-term annealing[30,31] and that oxidation of the chromium-rich carbides by the moving oxidation front can involve their embedding into the inner oxide layer.[15] The detection of carbides in the current study only directly beneath the inner oxide layer suggests a local increase of their volume fraction either because of pronounced coarsening or preferential carbide formation because of increased chromium and carbon concentrations at the interface between the inner oxide layer and the alloy.

2. *Austenitic superheater tubes*

Clear phase identification on the steamside surface of the austenitic steel TP347H is less straightforward compared with the X20CrMoV12-1 steel because stronger overlap and more pronounced asymmetries of the measured diffraction lines were observed (Figure 6). Furthermore, steamside oxidation of the austenitic steel was found to be considerably influenced by the exposure conditions of the tubes and the characteristics of the initial microstructure of the steel surface; an example is shown in Figure 6. For the three different TP347H samples, the formation of hematite seems to be similar, and the measured Bragg angles correspond to the theoretical values for stoichiometric phase composition. However, considerable differences were observed for the spinel phase: Overlapping diffraction lines indicate that solid solutions rather than solely pure magnetite formed on the steamside surfaces of the steel. For the coarse-grained austenitic steel TP347H (samples TP-CG-1 and -2), a shift of the Bragg angles toward lower values

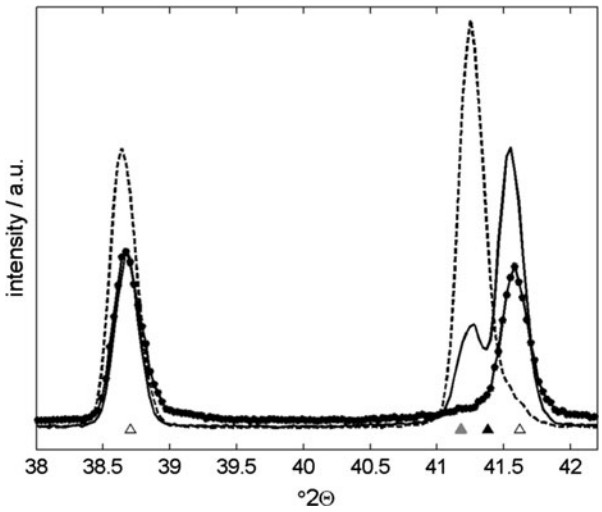


Fig. 6—Example of diffraction line profiles measured for various samples of TP347H superheater tubes with different microstructure and position within the superheater loop (*i.e.,* with and without heat flux): coarse-grained TP347H (sample TP-CG-2, black line), coarse-grained TP347H (sample TP-CG-1, dotted line), and fine-grained TP347H (line with marker). The theoretical positions corresponding to hematite (open triangle), magnetite (black triangle), and $MnCr_2O_4$ (gray triangle) are marked.

indicates the presence of manganese in the spinel, which agrees with EDS surface measurements. Compositional changes of the spinel phase occur as a function of depth as indicated by pronounced asymmetries and a shift of the diffraction line maxima (Figure 7). Directly at the surface, the steamside oxide consists of manganese-containing spinel (in addition to hematite). Approximately 5 $\mu$m beneath the surface, *i.e.,* after the first removal step, the measurements indicate clearly the coexistence of two spinel phases: pure magnetite and a solid solution spinel with manganese and chromium. With increasing distance from the surface, the volume fraction of pure magnetite decreases, and the oxide consists mainly of manganese- and chromium-containing spinel. Grazing incidence measurements confirm this depth dependence of the spinel phases for coarse-grained TP347H.

Similar to the observations for the X20CrMoV12-1 and the coarse-grained TP347H superheater tubes, also for the fine-grained austenitic steel TP347H-FG the composition of the hematite phase remains unchanged in depth (depth-dependent measurements with grazing incidence measurements and after various removal steps indicate no change of the measured Bragg angles, which correspond well with the theoretical values). In contrast to the previously mentioned coexistence of two spinel phases with different composition observed for coarse-grained TP347H, a pure magnetite phase was not observed for the fine-grained steel TP347H, and throughout the whole oxide scale, the spinel phase consists of solid solutions. To prove whether the absence of pure magnetite is a local effect and related to possible inhomogeneity or spallation, additional measurements were carried out at several positions on the fine-grained austenitic superheater tube, but magnetite was not

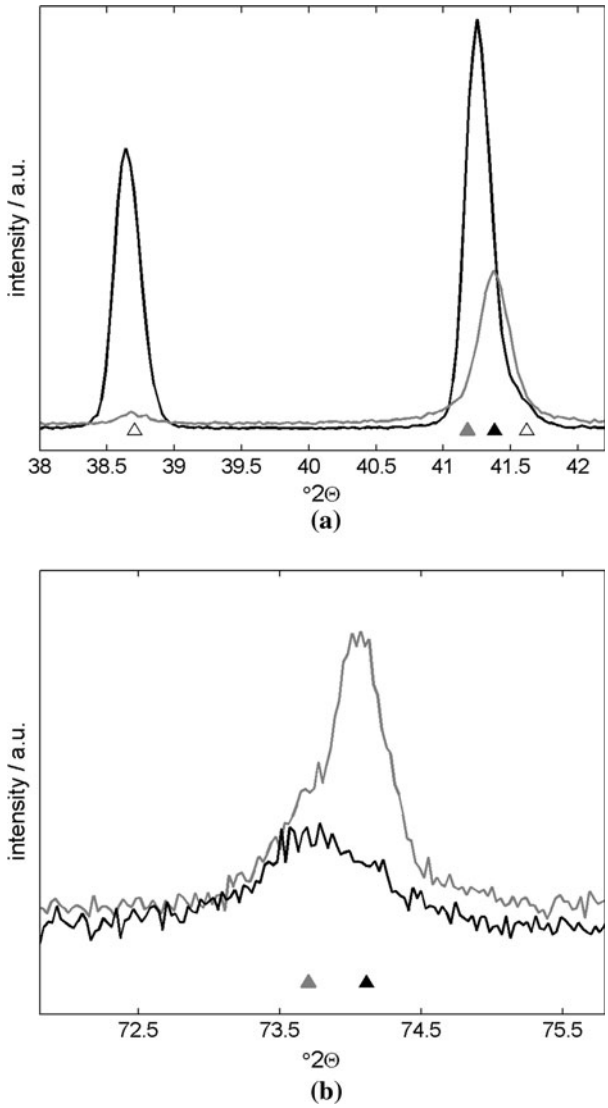


Fig. 7—Selected diffraction lines measured for coarse-grained TP347H (sample TP-CG-1) indicating considerable changes of the oxide in depth: original surface (black line in (*a*)), after removal of 5 $\mu$m (gray lines in (a) and (*b*)), and after removal of 25 $\mu$m (black line in (b)). The theoretical positions corresponding to hematite (open triangle), magnetite (black triangle), and $MnCr_2O_4$ (gray triangle) are marked.

detected. The chemical composition of the spinel phase changes considerably with depth. Enhanced diffusion because of the higher density of grain boundaries in the fine-grained austenitic steel obviously yields solid solutions of various alloying elements (Ni, Mn, and Cr) in the spinel phase. However, unambiguous phase identification is hindered considerably by strongly overlapping peaks and pronounced preferred crystallographic orientations. As a result, mostly individual diffraction lines rather than a set of reflections corresponding to the same phase can be found. Even the application of different wavelengths in combination with grazing incidence measurements did not allow clear phase identification. An example of changing phase compositions with depth is shown in Figure 8.

B. *Phase-Specific Residual Stresses on the Steamside of Superheater Tubes*

XRD stress analysis on the inner side, *i.e.,* the concave surfaces, of the tubes required cutting the tubes into rings, which allowed the X-ray beam to enter and leave the sample through the ring openings. Cutting rings from the tube should not have affected their circumferential stresses. However, stress relaxation in longitudinal direction cannot be excluded, in particular, because of the limited widths of the cut rings, which was required for avoiding shading effects in the X-ray path. Accordingly, the measurements revealed longitudinal stresses for the ring rather than the entire tube.

In addition to the aforementioned difficulties and limitations related to stress analysis on the steamside of the superheater tubes, meaningful measurements on the concave side of the ring samples were challenging because accurate positioning of the inner surface of the rings was hindered by the sample geometry, and commonly applied sample positioning tools cannot be used in this case. Therefore, nickel powder was applied on the concave surface of the samples and used for accurate height positioning of the samples in the diffractometer. Despite the careful and extensive alignment of each sample, the measurements on the inner side of the rings, including tilting the samples as required for stress analysis, were challenging; relatively large standard deviations for the regression lines in the $\sin^2\psi$ plots indicate the measurement difficulties. Nevertheless, the measurements revealed distinct differences in the state of residual stresses for the steamside oxides on ferritic-martensitic and austenitic steel tubes (Table IV).

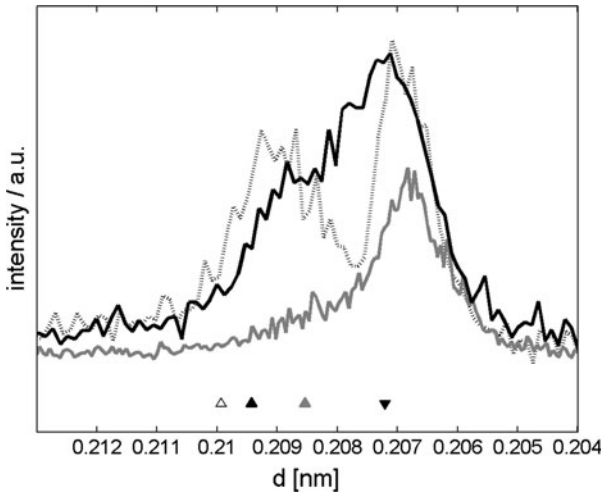


Fig. 8—Selected diffraction lines measured for fine-grained TP347H (sample TP-FG) on one and the same location with different X-ray penetration depth $\tau$: Co-K$\alpha$ radiation, $\tau \approx 9$ $\mu$m (dotted line), Cr-K$\alpha$ radiation, $\tau \approx 4$ $\mu$m (gray line), Co-K$\alpha$ with incidence angle of 10 deg, $\tau \approx 5.5$ $\mu$m (black line). The theoretical positions corresponding to magnetite (open triangle), $(Ni,Fe,Mn)O_4$ (gray triangle), $(Fe,Cr)O_4$ (black triangle), and the substrate (triangle downward) are marked.

For the ferritic-martensitic steel X20CrMoV12-1, the measured lattice strain increases linearly with $\sin^2\psi$ for both the hematite and the magnetite phases, and accordingly, tensile stresses were determined for both phases. In contrast, the steamside oxides on coarse-grained austenitic steel tubes TP347H-CG were found to be under compressive stress as obtained from the linear decrease of the measured lattice strain with $\sin^2\psi$. For the fine-grained austenitic steel TP347H-FG, nonlinear lattice strain distributions were determined on the inner side of the ring samples, *i.e.,* for the steamside oxides. Figure 9 shows an example of such a $\sin^2\psi$-plot (measurements on other fine-grained TP347 samples, in addition to the sample of the current work, confirmed this result), which indicates that no linear regression of the measured data for stress calculation can be applied.

The most common reasons for deviations from linearity in the $\sin^2\psi$ plot (crystallographic texture, grain statistics, stress gradients, and shear stresses[22]) do not apply to the current samples. Although grains are not oriented randomly, the influence of the crystallographic texture is not strong, and reasonably good diffracted intensities were obtained over the whole $\psi$-range. More important is the influence of chemical inhomogeneities as a result of enhanced diffusion of alloying elements in the fine-grained austenitic steel. This may result in both in-plane and in-depth variations of the local phase compositions and, hence, inevitable uncertainties in peak profile fitting and deconvolution. The observed asymmetric line profiles for the fine-grained TP347 samples support this interpretation but indicate also that XRD residual stress analysis on those samples has limited meaning (in addition to the difficulties related to the sample geometry,[32,33] as mentioned previously).

The clear differences in the stress state of the two coarse-grained steels, *i.e.,* tensile stresses for the ferritic-

**Table IV. Residual Stresses for the Hematite (226 reflection) and Magnetite (731 reflection) Phases in the Steamside Oxides on the Superheater Tubes**

| | $\sigma_1$ (MPa) | | $\sigma_2$ (MPa) | |
|---|---|---|---|---|
| | Hematite | Magnetite | Hematite | Magnetite |
| X20-1 | +318 ± 40 | +467 ± 83 | +212 ± 101 | +520 ± 165 |
| X20-2 | +459 ± 101 | +466 ± 35 | +176 ± 46 | +219 ± 23 |
| TP-FG | 2 slopes in $\sin^2\psi$-plots (cf. Fig. 9) | | | |
| TP-CG-1 | * | –483 ± 157 | * | –162 ± 176 |
| TP-CG-2 | –300 ± 119 | –503 ± 115 | –777 ± 94 | –592 ± 124 |

*The measured intensity was not sufficient for stress evaluation.

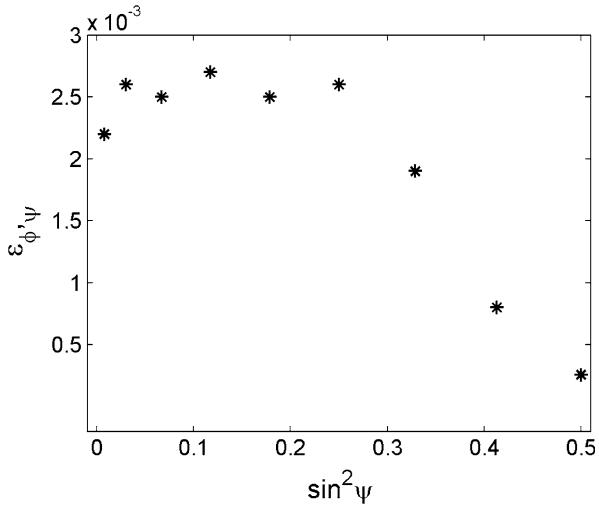


Fig. 9—Typical lattice strain distribution measured on the steamside, *i.e.,* the inner side, of ring samples of the fine-grained austenitic steel tube (example shown: sample TP-FG, $\varphi = 0$, hematite).

martensitic steel X20CrMoV12-1 and compressive stresses for the austenitic steel TP347H, agree with the expected stress formation according to the thermal expansion of the oxides and steels during cooling from the operating temperature of the superheater tubes. An exact calculation of thermal stresses fails for magnetite because of the strong temperature dependence of its linear thermal expansion coefficient within the expected temperature range,[23] but the sign of thermal stresses agrees with the measurements for both steels. Although it seems that the oxide scale on the steamside of the superheater tubes is affected by thermal stresses, the additional contribution of other influences on the stresses in the oxide film (like geometry- and exposure-dependent growth stresses, creep, internal oxidation or solid solution of oxygen in the steel) cannot be evaluated based on the current data. Regardless of their origin, the nature of stresses determined for the steamside oxides formed on both types of steel can be related to the different resistance against spallation of the steamside oxides: Oxides on ferritic-martensitic steels do not suffer from serious spallation, whereas spallation is observed mainly for oxides on austenitic steels.[3] Compressive stresses in the oxide, as indeed measured for the steamside oxides formed on the austenitic stainless steel, favor cracking and spallation by buckling and wedging.[20,23]

## IV. CONCLUSIONS

The formation of steamside oxides during long-term, high-temperature exposure of superheater tubes in thermal power plants, which usually is investigated solely by microscopic analysis, is studied by means of XRD. The feasibility of qualitative phase analysis and residual stress analysis for the characterization of steamside oxidation on real plant exposed tubes was proven. For studying oxide growth, XRD is normally applied straightforwardly on geometrically and compositional well-defined model samples, which were intentionally heat treated in the laboratory under simplified conditions to mimic plant exposure. The current work applies XRD to real plant-exposed superheater tubes, which is challenging because of (1) the steamside oxides formed on the inner side of the tubes are difficult to access by the X-ray beam, (2) the limited accessibility in combination with the concave surface curvature hinders alignment of the sample position into the centre of the diffractometer, and (3) possible local heterogeneities with respect to the chemical and phase compositions within the diffracting volume as a result of diffusion, spallation, or unreported service exposure complicates the interpretation of the XRD data. Despite all difficulties and limitations, the XRD results obtained from qualitative phase analysis and the analysis of internal stresses on real plant-exposed superheater tubes contributed to the understanding of the formation and spallation of steamside oxides on the investigated superheater tubes.

Essential differences with respect to the steamside oxides formed on ferritic-martensitic steel X20CrMoV12-1 and on lean austenitic stainless steel TP347H were observed. An XRD phase analysis revealed the presence of hematite ($Fe_2O_3$) on the outermost surface on the inner side of the tubes facing the steam atmosphere. For both types of steel, the hematite layer was found to have stoichiometric composition regardless of the exposure conditions in the power plant. In larger depths, beneath the hematite layer, the steamside oxides contain a spinel phase, which consisted of either pure magnetite ($Fe_3O_4$) or magnetite with solid solutions of the steel alloying elements (mainly, Cr and Mn). In particular, for the fine-grained austenitic steel, strong peak asymmetries were observed indicating the coexistence of various solid solution spinels, which considerably hinder thorough phase identification. A residual stress analysis on ring samples of the superheater tubes revealed that the state of stresses in the steamside oxides depends mainly on the type of steel: Tensile stresses form in both the hematite and magnetite phases on ferritic-martensitic superheater tubes, whereas the steamside oxides on coarse-grained austenitic tubes are under compressive stress, which can explain dramatic spallation of steamside oxides on austenitic steel.

An XRD analysis on steamside oxides on plant-exposed superheater tubes considerably supplements the microscopic analysis of the grown oxides, and it should be applied as an additional rather than an alternative characterization method for the following reasons. Straightforward phase identification for the oxide scale solely based on X-ray diffraction is limited because slight differences of the chemical composition and corresponding changes of the unit cell parameters for phases comprising the same crystal structure (*e.g.,* spinel containing various alloying elements in solid solution) cannot be resolved. XRD provides absorption-weighted averages originating from a relatively large diffracting volume, and hence, local heterogeneities cannot be revealed. Supplementing information on the local distribution of diffusing species by means of, *e.g.,* EDS, is

therefore of particular importance. Furthermore, the information on the local distribution of individual phases in a multiphase material gained solely from XRD depends on the used technique: From a single measurement indicating the simultaneous presence of several phases within the diffracting volume, it cannot be concluded whether the various phases are arranged as multilayers on top of each other or as local precipitates within a matrix. A diffraction analysis with systematic variations of the X-ray penetration depth by grazing incidence measurements, however, allows depth-resolved phase analysis, and hence, in-depth gradients in terms of either gradual changes of the stoichiometry of a certain phase or several phases formed in different depths can be evaluated. Although the complementary information from XRD and microscopic techniques is helpful for thorough phase analysis, the ability to determine residual stresses is a clear advantage of XRD. Phase-specific stresses in the near-surface region are available by conventional X-rays (as shown in the present study), but the nondestructive analysis of stress gradients in larger depths would require the use of synchrotron radiation.

The current examples of XRD analysis on real superheater tubes also indicate that comparative studies applying XRD routinely on replaced superheater tubes as an initial inspection tool can help to define specific locations for dedicated microscopic studies. Often, plant-exposed superheater tubes show some variations of the appearance, color, and roughness of steamside oxides, which can be observed by macroscopic visual inspection on various locations on the tube. For such odd-looking locations, XRD nevertheless confirmed the presence of identical phases as in other locations. This finding indicates that solely visual evaluation of the oxide scale appearance can be misleading, and for the current work, the reproducible phase identification regardless of the position on one and the same tube emphasizes the informational value of the XRD results.

## ACKNOWLEDGMENT

The authors thank Värmeforsk (Thermal Engineering Research Association) Sweden, for financial support (project M4-312).

## REFERENCES

1. I.G. Wright, A.S. Sabau, and R.B. Dooley: *Mater. Sci. Forum*, 2008, vols. 595–598, pp. 387–95.
2. S.R.J. Saunders and L.N. McCartney: *Mater. Sci. Forum*, 2006, vols. 522–523, pp. 119–28.
3. O.H. Larsen, R.B. Frandsen, and R. Blum: *VGB Power Tech.*, 2004, vol. 84, pp. 89–96.
4. A.N. Hansson and M. Montgomery: *Mater. Sci. Forum*, 2006, vols. 522–523, pp. 181–88.
5. A.N. Hansson, M. Montgomery, and M.A.J. Somers: *Oxid. Met.*, 2009, vol. 71, pp. 201–18.
6. J. Jianmin, M. Montgomery, O.H. Larsen, and S.A. Jensen: *Mater. Corros.*, 2005, vol. 56, pp. 542–49.
7. I.G. Wright and R.B. Dooley: *Int. Mater. Rev.*, 2010, vol. 55, pp. 129–67.
8. A.N. Hansson and M. Montgomery: *Proc. of 9th Liege Conf.: Materials for Advanced Power Engineering*, Eds. J. Lecomte-Beckers, Q. Contrepois, T. Beck, and B. Kuhn, Forschungszentrum Jülich GmbH, Jülich, Germany, 2010, pp. 1022–31.
9. M. Montgomery, A.N. Hansson, T. Vilhelmse, and S.A. Jensen: *Mater. Corros.*, 2011, in press.
10. M.M. Rahman, J. Purbolaksono, and J. Ahmad: *Eng. Fail. Anal.*, 2010, vol. 17, pp. 1490–94.
11. D.L.C. Neves, J.R de Carvalho Seixas, E.B. Tinoco, A. da Cunha Rocha, and I. de Cerqueira Abud: *Mater. Res.*, 2004, vol. 7, pp. 155–61.
12. A.S. Sabau and I.G. Wright: *Oxid. Met.*, 2010, vol. 73, pp. 467–92.
13. A.S. Sabau and I.G. Wright: *J. Appl. Phys.*, 2009, vol. 106, pp. 023503-1–023503-8.
14. M. Montgomery, S.A. Jensen, A. Hansson, O. Biede, and T. Vilhelmsen: *Proc. of 9th Liege Conf.: Materials for Advanced Power Engineering*, Eds. J. Lecomte-Beckers, Q. Contrepois, T. Beck, and B. Kuhn, Forschungszentrum Jülich GmbH, Jülich, Germany, 2010, pp. 1096–1105.
15. J. Zurek, E. Wessel, L. Niewolak, F. Schmitz, T.-U. Kern, L. Singheiser, and W.J. Quadakkers: *Corros. Sci.*, 2004, vol. 46, pp. 2301–17.
16. W. Christl, A. Rahmel, and M. Schütze: *Oxid. Met.*, 1989, vol. 31, pp. 35–69.
17. D.R. Clarke: *Acta Mater.*, 2003, vol. 51, pp. 1393–1407.
18. F.N. Rhines and J.S. Wolf: *Metall. Trans.*, 1970, vol. 1, pp. 1701–10.
19. C. Zhou, H. Ma, and L. Wang: *Oxid. Met.*, 2009, vol. 71, pp. 335–41.
20. H.E. Evans: *Int. Mater. Rev.*, 1995, vol. 40, pp. 1–40.
21. R. Krishnamurthy and D.J. Srolovitz: *Acta Mater.*, 2004, vol. 52, pp. 3761–80.
22. V. Hauk: *Structural and Residual Stress Analysis by Non-Destructive Methods*, Elsevier, Atlanta, GA, 1997.
23. M. Schütze: *Protective Oxide Scales and their Breakdown, Series on Corrosion and Protection*, Wiley, New York, NY, 1991.
24. Landolt-Börnstein: *Numerical Data and Functional Relationships in Science and Technology*, vol. 11, Springer-Verlag, Germany, 1979.
25. X. Luo, R. Tang, C. Long, Z. Miao, Q. Peng, and C. Li: *Nucl. Eng. Tech.*, 2008, vol. 40, pp. 147–54.
26. H.J. Yearian, J.M. Kortright, and R.H. Langenheim: *J. Chem. Phys.*, 1954, vol. 22, pp. 1196–98.
27. G.C. Allen, K.R. Hallam, and J.A. Jutson: *Powder Diffr.*, 1995, vol. 10, pp. 214–20.
28. P. Perrot: *Landolt-Börnstein, New Series IV/11D3*, Springer, 2008, pp. 1–27.
29. A.N. Hansson, K. Pantleon, F.B. Grumsen, and M.A.J. Somers: *Oxid. Met.*, 2010, vol. 73, pp. 289–309.
30. Z.-F. Hu and Z.-G. Yang: *Mater. Sci. Eng. A*, 2004, vol. 383, pp. 224–28.
31. D.A. Skobir, M. Godez, A. Nagode, and M. Jenko: *Surf. Interface Anal.*, 2010, vol. 42, pp. 717–21.
32. M. Francois, B. Dionnet, J.M. Sprauel, and F. Nardou: *J. Appl. Cryst.*, 1995, vol. 28, pp. 761–67.
33. T. Oguri, K. Murata, and Y. Sato: *J. Strain Anal.*, 2003, vol. 38, pp. 459–68.